INORGANIC CHEMISTRY
FRONTIERS

RESEARCH ARTICLE

View Article Online
View Journal | View Issue

Check for updates

Cite this: *Inorg. Chem. Front.*, 2023, **10**, 2645

# Stable self-trapped broadband emission from an organolead halide coordination polymer with strong layer corrugation and high chemical robustness†

Ruonan Xi,‡ Yilin Jiang,‡ Yukong Li, Jinlin Yin and Honghan Fei *

Received 15th February 2023,
Accepted 23rd March 2023

DOI: 10.1039/d3qi00283g

rsc.li/frontiers-inorganic

Layered organolead halides are an emerging class of self-trapped emitters, in which the unique corrugated structures are critical to afford out-of-plane distortions for self-trapping. However, the labile corner halide species are often more exposed in corrugated layers, posing the trade-off relationship between structural corrugation and chemical robustness. Herein, we report a layered architecture consisting of inorganic $[Pb_2Cl_2]^{2+}$ slabs and interlamellar 4,5-imidazoledicarboxylate struts, exhibiting large Stokes-shifted broadband emission originating from self-trapped excitons. The coordination-assembly hybrid possesses both high structural integrity and heavily corrugated lead chloride layers, therefore affording ultrastable and efficient self-trapped photoluminescence. The broadband emission is well retained after a variety of chemical treatments and maintains the spectral profile for at least 168 h upon continuous UV irradiation under ambient conditions, superior to conventional ionic structures for halide perovskites. The photophysical carrier dynamics and the exciton self-trapping process of our layered material have been clarified by a variety of photophysical studies including ultrafast transient absorption spectroscopy.

## Introduction

Organolead halide hybrids are an emerging class of crystalline materials with excellent photophysical properties, therefore showing optoelectronic applications in light-emitting diodes,[1–5] photovoltaic solar cells,[6–9] and photodetectors.[10–12] Among them, a selected group of organolead halide perovskites have attracted widespread attention for their unique emissions from self-trapped excitons (STEs), which play the role of defective excited states to afford a large Stokes shift and broadband emission.[13] Mechanistic studies indicate that the formation of STEs originates from the structural distortion of lead halide sublattices, especially the out-of-plane distortion of halide species.[14] Therefore, a variety of studies have been performed to enhance the lamellar corrugation of lead halide layered structures, for example 2 × 2 and 3 × 3 "rooflike" corrugated (110)-oriented perovskites.[15,16] Besides tuning the layer corrugation, lowering the inorganic dimensionality is another widely used strategy to promote the structural deformation and the formation of STEs.[17,18]

Although strong layer corrugation increases the ratio of the integrated intensities of the broad STE emission to the narrow emission from free excitons, the corner halide species of wavy lead halide slabs are often more exposed and are subject to hydrolysis.[19] The corner-ending halides are susceptible to be replaced by high-polar protic molecules, which is the key origin of intrinsic structural instability for halide perovskites.[20,21] Therefore, the vast majority of corrugated organolead halide perovskites have a low formation energy, and are prone to undergo rapid degradation in the presence of a protic environment including air moisture.[19] The formation of all-inorganic perovskite structures is effective for enhancing the structural stability, but the substitution of organoammonium by inorganic $Rb^+/Cs^+$ cations sacrifices the structural tunability to regulate the corrugation of inorganic sheets.[22] Therefore, it remains a great challenge to overcome the trade-off relationship between the strong structural corrugation and high chemical robustness in layered lead halide hybrids, in order to realize long-term ultrastable STE emission for widespread applications.

Our group focused on using organocarboxylates as the interlamellar pillars to construct a family of layered organolead halide coordination polymers, which exhibit high robustness over a wide range of pH values and under aqueous boiling

---

*Shanghai Key Laboratory of Chemical Assessment and Sustainability, School of Chemical Science and Engineering, Tongji University, 1239 Siping Rd., Shanghai 200092, P. R. China. E-mail: fei@tongji.edu.cn*

† Electronic supplementary information (ESI) available: Experimental details and additional characterization. CCDC 2240115. For ESI and crystallographic data in CIF or other electronic format see DOI: https://doi.org/10.1039/d3qi00283g

‡ These authors contributed equally to this work.

conditions.[18,19,23–26] This is largely ascribed to the $Pb^{2+}$-carboxylate coordination motifs in our layered architectures that afford enhanced structural integrity, superior to the ionic bonded structures for perovskites.[19] In order to advance the elastic deformation and the role of STEs, great efforts have been made to decrease the inorganic dimensionality of lead halide sublattices in the coordination networks.[27–29] It is noticed that the out-of-plane distortion of halide species is critical to the contribution of the broad STE emission and the absolute photoluminescence quantum efficiency (PLQY) of up to 72%.[30] However, in this class of ultrastable layered coordination polymers, the vast majority of lead halide slabs possess slight layer corrugation. Therefore, it is intriguing to manipulate the distortion of lead halide layers and investigate the structure–property relationship based on STEs.

Herein, we have employed 4,5-imidazoledicarboxylate ($imdc^{2-}$) as the interlamellar coordinating linker to pillar $[Pb_2Cl_2]^{2+}$ layers, endowing a lead halide coordination polymer with an inorganic lamellar structure. Interestingly, the resulting layered architecture exhibits both high chemical stability and strong corrugation in $[Pb_2Cl_2]^{2+}$ layers, affording broad photoluminescence ranging from 400 to 650 nm and a large Stokes shift of 183 nm. Importantly, our layered coordination material exhibits excellent long-term emission stability under continuous UV-irradiation conditions, superior to conventional corrugated (110)-oriented layered perovskites.[31] The intrinsic structural distortion of layered $[Pb_2Cl_2]^{2+}$ sublattices enables strong interactions between excitons and phonons, thus promoting the formation of STEs. A variety of photophysical experiments, including temperature-dependent steady-state and transient-state PL studies and ultrafast transient absorption (TA) spectroscopy, give a deep mechanistic understanding of the exciton self-trapping and detrapping dynamics.

## Experimental section

### Materials

All starting reagents and solvents were purchased from commercial sources and used without further purification, including lead chloride ($PbCl_2$, 99.0%, Aladdin), 4,5-imidazoledicarboxylate ($C_5H_4N_2O_4$, >97.0%, Aladdin), hydrochloric acid (HCl, 38%, SCRC), lead acetate trihydrate ($Pb(Ac)_2{\cdot}3H_2O$, 99.5%, Aladdin), 1-(3-aminopropyl)imidazole (97%, TCI), acetonitrile ($CH_3CN$, >99.0%, Adamas), *N*,*N*′-dimethylformamide (DMF, >99.5%, Adamas), ethanol (EtOH, >99.5%, Adamas), dichloromethane (DCM, >99.5%, Adamas) and perchloric acid ($HClO_4$, 70% in $H_2O$, Adamas). Deionized water was obtained from a Barnstead Pacific RO water purification system.

### Synthesis

**$[Pb_2Cl_2]^{2+}(imdc^{2-})$ (TJU-19).** A mixture of 0.250 g of $PbCl_2$ (0.9 mmol), 0.047 g of 4,5-imidazoledicarboxylate (0.3 mmol), 150 μL of perchloric acid ($HClO_4$, 1.8 mmol) and 8 mL of solvents of $H_2O$/MeCN (2 : 1 v : v) were added into a 15 mL Teflon-lined autoclave, followed by 15 min magnetic stirring for sufficient dispersion. The autoclave was then sealed into a stainless-steel vessel and heated statically at 120 °C for 72 h. Upon the autoclave cooling to room temperature, colorless plate-like crystals were isolated by vacuum filtration, rinsed with EtOH, and then dried at 60 °C for 10 h (yield: 128 mg, ~45% based on Pb). Elemental analysis: calculated C, 9.39%; H, 0.31%; N, 4.38%; found C, 9.38%; H, 0.29%; N, 4.35%.

***N*-(3-Aminopropyl)-imidazole tetrachlorolead perovskite (1).** The material is synthesized according to a previous literature study with slight modifications.[31] $Pb(Ac)_2{\cdot}3H_2O$ (3.79 g, 0.01 mol) and 1-(3-aminopropyl)-imidazole (1.25 g, 0.01 mol) were added into an aqueous HCl solution (38%, 150 mL) in a clean 500 mL round-bottom flask. Clear solutions were obtained after 50 min of heating. After 12 h, colorless single crystals were isolated by slowly evaporating the solvent at 40 °C.

### Single-crystal X-ray crystallography

Single-crystal data of TJU-19 were collected on a Bruker D8 Venture diffractometer equipped with a Photon III detector. Further details of the crystallographic data and structural refinement are summarized in Table S1.† Diffraction data were processed using the APEX3 software package, integrated using SAINT, and corrected for absorption effects using SADABS. The space group was determined by systematic absences, *E*-statistics, agreement factors for equivalent reflections, and successful refinement of the structure. The structure was solved by direct methods and expanded routinely, and refined by full-matrix least-squares analysis of $F^2$ against all reflections using the SHELXTL software package. All non-hydrogen atoms were refined with anisotropic thermal displacement parameters. Thermal parameters for hydrogen atoms were tied to the isotropic thermal parameter of the atoms to which they are bound.

### Stability studies

**Chemical stability.** ~100 mg of the as-synthesized TJU-19 crystals were incubated under aqueous conditions (pure deionized water, a HCl solution of pH = 3, and a NaOH solution of pH = 11) and organic solvents (including DCM, EtOH and DMF) at room temperature for 24 h. Then, the samples were isolated by centrifugation, followed by PXRD and photophysical measurements.

**Photostability.** The as-synthesized TJU-19 crystals and layered perovskite **1** crystals were irradiated continuously using a 365 nm UV lamp (14 mW $cm^{-2}$) under ambient conditions (~60% relative humidity, room temperature) for 7 days, and were monitored by PXRD and photophysical measurements. Moreover, TJU-19 crystals were irradiated using a 300 W Xe lamp for 12 h, followed by PXRD and photophysical studies.

### Instrumental characterization

Unless otherwise stated below, TJU-19 for instrumental characterization is in the form of manually ground powders. Powder X-ray diffraction (PXRD) analysis was performed on a Bruker D2 Phaser X-ray diffractometer equipped with a Cu sealed tube

($\lambda$ = 1.54184 Å) at 30 kV and 10 mA with a scan speed of 1 s per step, a step size of 0.02° in $2\theta$, and a $2\theta$ range of 5–40°. Elemental analysis (EA) for C/H/N was performed using a Varian EL III element analyzer. TGA was carried out on a TGA Q5000 differential thermal analyzer. The samples were heated in a $N_2$ stream from 25 to 800 °C with a heating rate of 10 °C $min^{-1}$. Ultraviolet–visible (UV–vis) absorption spectroscopy was performed on a Shimadzu UV-2600 ultraviolet–visible spectrophotometer equipped with an integrating sphere, using 100% $BaSO_4$ as the reflectance standard for all measurements. Femtosecond TA spectroscopy was performed on a Helios pump–probe system (Ultrafast Systems LLC) combined with an amplified femtosecond laser system (Coherent), by dispersion of TJU-19 powders in ethylene glycol.

### Photoluminescence measurements

The excitation and emission spectra, PLQYs, temperature-dependent emission spectra, and time-resolved PL decay were recorded on a Horiba Fluorolog setup (Fluorolog-3C-111) in reflection mode. The emission spectra were obtained under 337 nm excitation, using a 1 nm scan step and 5 nm slit width. For PLQY measurements, samples were excited at 340 nm light output from a 450 W Xe lamp with an integrating sphere ($BaSO_4$ coating) in a single-photon counting mode. The PLQYs are reported based on the average of multiple independent samples. The PLQYs were calculated using the equation: $\varphi = k_f/k_a$, in which $k_f$ and $k_a$ are the number of emitted and absorbed photons, respectively. Excitation light with a specific wavelength (340 nm) for the time-resolved emission was provided by an EPL-340PS pulsed diode laser, and the monitored emission wavelength was 520 nm.

### Computational methods

First-principles calculations based on density functional theory were performed. The band structure and DOS of TJU-19 were calculated using VASP,[32,33] where the Perdew–Burke–Ernzerhof generalized gradient approximation (GGA) method is applied.[34] The electrical conductivity and the Seebeck coefficient with respect to charge carrier density were calculated based on the Boltzmann transport theory as implemented in BoltzTraP.[35] The cut-off energy for the plane wave basis was set to 450 eV. A Γ-centered Monkhorst–Pack[36] 4 × 4 × 4 *k*-mesh was adopted to sample the Brillouin zone. For electrical transport calculations, the *k*-mesh was further increased to 9 × 9 × 9. All the systems were fully relaxed before the calculations of electronic structures, in which spin–orbit coupling effects were included.

## Results and discussion

The solvothermal synthesis of $PbCl_2$ and $H_3$imdc in $H_2O$/MeCN affords colorless plate-like crystals of $[Pb_2Cl_2]^{2+}$(imdc$^{2-}$), which we denote as TJU-19 (TJU = Tongji University). The addition of perchloric acid during the synthesis is essential, which acts as a strong acid to tune the pH as well as a mineralizer for hydrofluoric acid in zeolite synthesis.[37] The high phase purity of TJU-19 is confirmed by a good matching between experimental powder X-ray diffraction (PXRD) and the simulated pattern from the single-crystal data (Fig. S1†). X-ray crystallography reveals that TJU-19 crystallizes in the triclinic crystal system, consisting of cationic $[Pb_2Cl_2]^{2+}$ layers that are coordinatively pillared by interlamellar imdc$^{2-}$ linkers (Fig. 1a). The cross-sectional crystallographic view of the $[Pb_2Cl_2]^{2+}$ layers shows stronger corrugation along the *b*-axis, which has not been observed in our previous layered coordination polymers (Fig. S3†). Each corrugated slab has a corrugation amplitude of 4.94 Å, and consists of an array of 1D lead chloride $[Pb_2Cl_2]^{2+}$ chains with three Pb atoms wide. The new 1D structural motif occupies a distorted square-grid-type Pb–Cl–Pb structure in a quasi-flat manner (Fig. 1b). An array of 1D chains are connected by interchain Pb–Cl bonds with bonding distances of 3.157 Å, forming corrugated $[Pb_2Cl_2]^{2+}$ layers (Fig. 1b). The layer corrugation in TJU-19 is analogous to the assembly of an array of $[Pb_2Cl_6]^{2-}$ chains in 2 × 2 corrugated (110)-oriented perovskites with a corrugation amplitude of 4.04 Å (Fig. 1c and Fig. S3†). The three or four adjacent $Pb^{2+}$

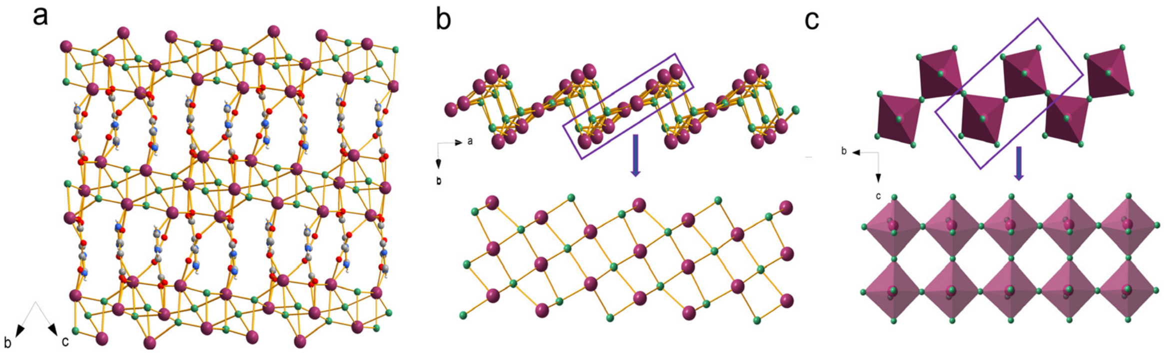

**Fig. 1** (a) Crystallographic view of TJU-19 along the *a*-axis. (b) Cross-sectional view of a single $[Pb_2Cl_2]^{2+}$ layer in TJU-19 (top) and the top view of a single chain from the $[Pb_2Cl_2]^{2+}$ layer in TJU-19 (bottom). (c) Cross-sectional view of a single $[Pb_2Cl_6]^{2-}$ layer in a 2 × 2 corrugated (110)-oriented perovskite **1** (top) and the top view of a single chain from the $[Pb_2Cl_6]^{2-}$ layer in perovskite **1** (bottom). Pb: purple, Cl: green, C: gray, N: dark blue, O: red, H: white.

sites residing in each $[Pb_2Cl_2]^{2+}$ layer of TJU-19 form a nearly flat layer, while the four crystallographic independent chlorides result in $\mu_3/\mu_4$-bridging to afford an average out-of-plane distortion of 39° (Fig. S12†). Meanwhile, each lead chloride $[Pb_2Cl_2]^{2+}$ sheet is coordinatively pillared by the imdc$^{2-}$ ligands, which reside in the interlamellar spacings (Fig. 1a). Notably, one carboxylate in imdc$^{2-}$ bridges the adjacent $[Pb_2Cl_2]^{2+}$ layers with two oxygens coordinated with the $Pb^{2+}$ centers in different layers, which afford a small interlayer spacing of ~6.38 Å. Based on C/H/N elemental analysis, the imidazole nitrogens of the organic component are protonated in TJU-19.

Ultraviolet–visible (UV–vis) diffuse reflectance spectroscopy confirms that the material has an absorption edge of up to 347 nm, affording the estimated band gap energy ($E_g$) of 3.64 eV (Fig. 2a). Owing to the analogous absorption behaviors, the clear absorption tail probably originates from the imdc$^{2-}$ ligands (Fig. S11†). The Tauc plot analysis confirms the direct band gap (Fig. S9†), which agrees with the DFT calculations of band structures that suggest the valence band maximum (VBM) and conduction band minimum (CBM) at the T point (Fig. 2b). The experimental band gap is slightly larger than the calculated value of 3.47 eV, owing to the well-known underestimation of the band gap by GGA functionals.[38] An isolated and narrow flat band is noticed near the CBM of TJU-19, which readily favors charge localization and promotes the formation of electron and hole polarons.[39] The calculated projected density of states (pDOS) of TJU-19 shows that the VBM is equally contributed by the Cl 3p orbitals and the imdc$^{2-}$ ligands (Fig. 2c and Fig. S13†).

The photophysical properties of TJU-19 were first studied by steady-state and transient-state PL spectroscopy. Upon 337 nm excitation, TJU-19 exhibits broadband yellow emission spanning from 400 nm to 650 nm with the emission maxima at 520 nm (2.38 eV), covering the majority of the visible spectrum (Fig. 3b). The strong broadband emission can be clearly observed using a 365 nm commercial UV light source (Fig. 3b, inset). Both the Stokes shift and the full-width at half-maximum (FWHM) of the broadband emission are determined to be 183 nm (1.29 eV) and 106 nm (0.51 eV), respectively (Fig. S8†). The large Stokes shift affords almost no overlap between the absorption spectra and emission spectra of TJU-19, suggesting the single-component broadband photoemitter overcoming the self-absorption problem. The color temperature and the CIE chromaticity coordinates are calculated to be 8800 K and (0.23, 0.45), respectively, corresponding to the yellowish green emission (Fig. 3c). Importantly, the PLQY of the broadband emission from TJU-19 is determined to be ~13%, which is largely ascribed to the structurally transmutable $[Pb_2Cl_2]$ sheets which will be discussed later. This value is higher than that of the vast majority of our previously reported layered lead halide coordination materials[18,25,26] and (110)-corrugated lead halide perovskites (*e.g.* 1.5% of (N-MEDA)$[PbBr_{2.8}Cl_{1.2}]$,[16] 9% of (EDBE)$[PbBr_4]$,[40] 1.05% of $(2meptH_2)PbCl_4$[41] and 4.84% of $[DAPMA]_2Pb_3Cl_{12}\cdot 2H_2O$[42]).

Given the efficient broadband emission from TJU-19, we sought to investigate its long-term stability under various chemical conditions. First, the high crystallinity and phase purity have been largely retained after the incubation of TJU-19 in a variety of aqueous solutions over a wide range of pH values (3–11) and in a variety of organic solvents including high-polar protic solvents, evidenced by PXRD and negligible loss in mass balance (Fig. 3a, d and e). However, a significant loss in mass balance is observed by incubation of the corrugated layered perovskite **1** in pure water for 24 h (Fig. S6†). Thermogravimetric analysis (TGA) indicates the high thermal stability of TJU-19 up to 200 °C (Fig. S5†). Indeed, we have performed the photophysical studies after incubating TJU-19 in aqueous solutions (Fig. 3d and g) and under organic conditions (*e.g.*, DMF, EtOH, and DCM) for 24 h (Fig. 3e and h). Intriguingly, no obvious change in both emission intensity and emission maxima was noticed. Moreover, the high photostability of TJU-19 was investigated by continuous UV irradiation (365 nm, 14 mW cm$^{-2}$) in air (~60% relative humidity) at room temperature for a total of 168 h. The structural integrity and the broadband emission were largely maintained, as monitored by PXRD and photoluminescence studies, respectively (Fig. 3f and i). Importantly, the (110)-

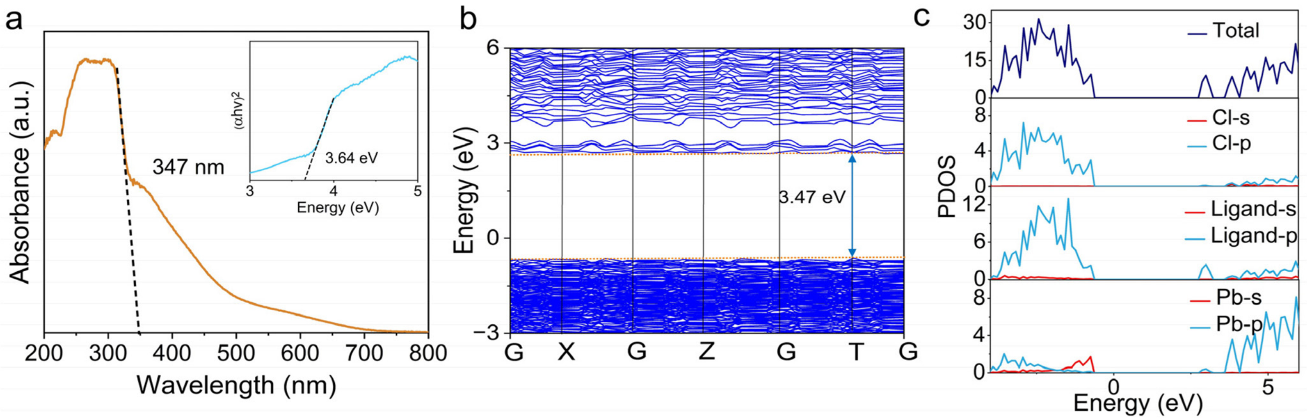

**Fig. 2** (a) UV-vis diffuse reflectance spectroscopy of TJU-19. The inset shows the estimated band gap according to the Tauc plot. (b) The calculated band structure of TJU-19. (c) pDOS of TJU-19.

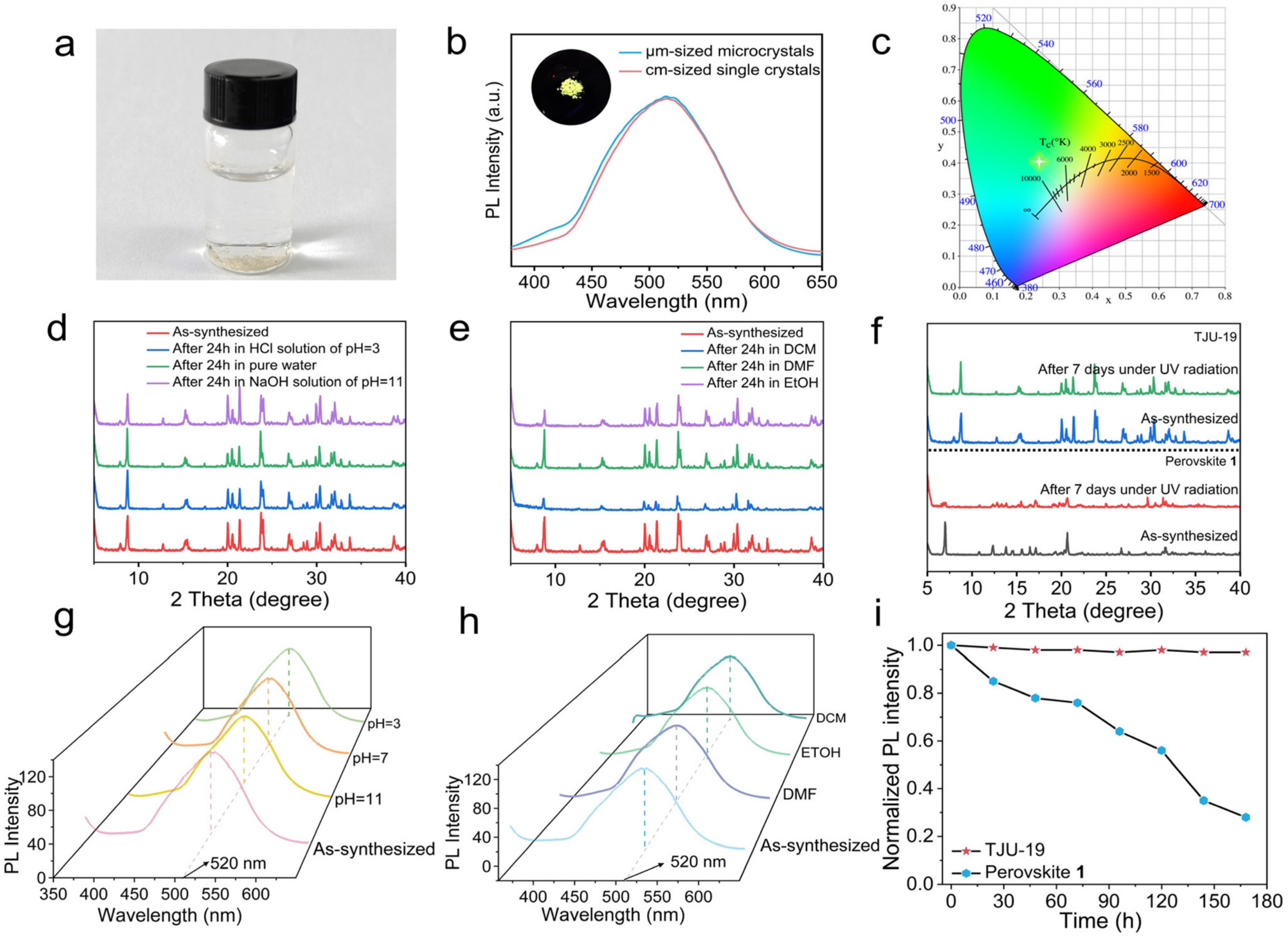

**Fig. 3** (a) Image of TJU-19 in pure deionized water after 24 h. (b) Photoluminescence spectra of the cm-sized single crystals (red) and μm-sized microcrystals (blue) of TJU-19 upon 337 nm excitation. The inset shows an image of TJU-19 under 365 nm UV light. (c) CIE chromaticity coordinates of TJU-19. (d and e) PXRD and (g and h) emission spectra of TJU-19 before and after chemical treatments. (f) PXRD of TJU-19 and (110)-oriented perovskite **1** before and after continuous illumination (14 mW $cm^{-2}$, 365 nm UV lamp) for 7 days in air. (i) Normalized emission intensity of TJU-19 and perovskite **1** under continuous illumination (14 mW $cm^{-2}$, 365 nm UV lamp) for 7 days in air (~60% RH, room temperature).

oriented layered perovskite **1** [31] was employed as the control material to perform the photostability studies under identical conditions. An ~17% decrease in the emission intensity was observed after irradiation of **1** in air for 24 h, and merely ~27% of the emission intensity was retained after continuous irradiation for 7 days (Fig. 3i). The photoluminescence quenching of **1** is attributed to the structural degradation evidenced by PXRD after 7d irradiation (Fig. 3f). Indeed, TJU-19 retains the structural integrity and the photoluminescence intensity even after continuous irradiation using a 300 W xenon lamp for 12 h (Fig. S15†). All these studies indicate that both the efficiency and the stability of STE-based emission from TJU-19 exceed those of the vast majority of (110)-oriented layered organolead halide perovskites, ascribed to the high corrugation of $[Pb_2Cl_2]^{2+}$ layers and the stable Pb-carboxylate coordination motif, respectively.

In order to further investigate the mechanism of broadband emission from TJU-19, variable-temperature steady-state photoluminescence and transient-state photoluminescence have been studied. First, the bulk single crystals and manually ground microcrystalline powders of TJU-19 showed analogous emission intensity and a spectral shape, agreeing with the intrinsic nature of emission and ruling out the contribution from the surface defects (Fig. 3b). Moreover, TJU-19 shows nearly identical emission profiles upon excitation at various wavelengths from 300 to 330 nm (Fig. S10†), suggesting the broadband emission originating from the single-source photoluminescence center. Temperature-dependent steady-state emission spectra indicated more intense and narrower emissive behaviors with temperature decreasing from 377 to 277 K, suggesting strong electron–phonon coupling in the lattice (Fig. 4a). Photoluminescence decay suggested an average short lifetime of 1.29 ns at room temperature and a long lifetime of 671.70 μs in 78 K for TJU-19 (Fig. 4b and c), again supporting the claim of the STE mechanism based on electron–phonon coupling in the deformable lattice. This is because the cryogenic temperature may limit the detrapping process of STEs, while the thermal equilibrium between the free excitons and

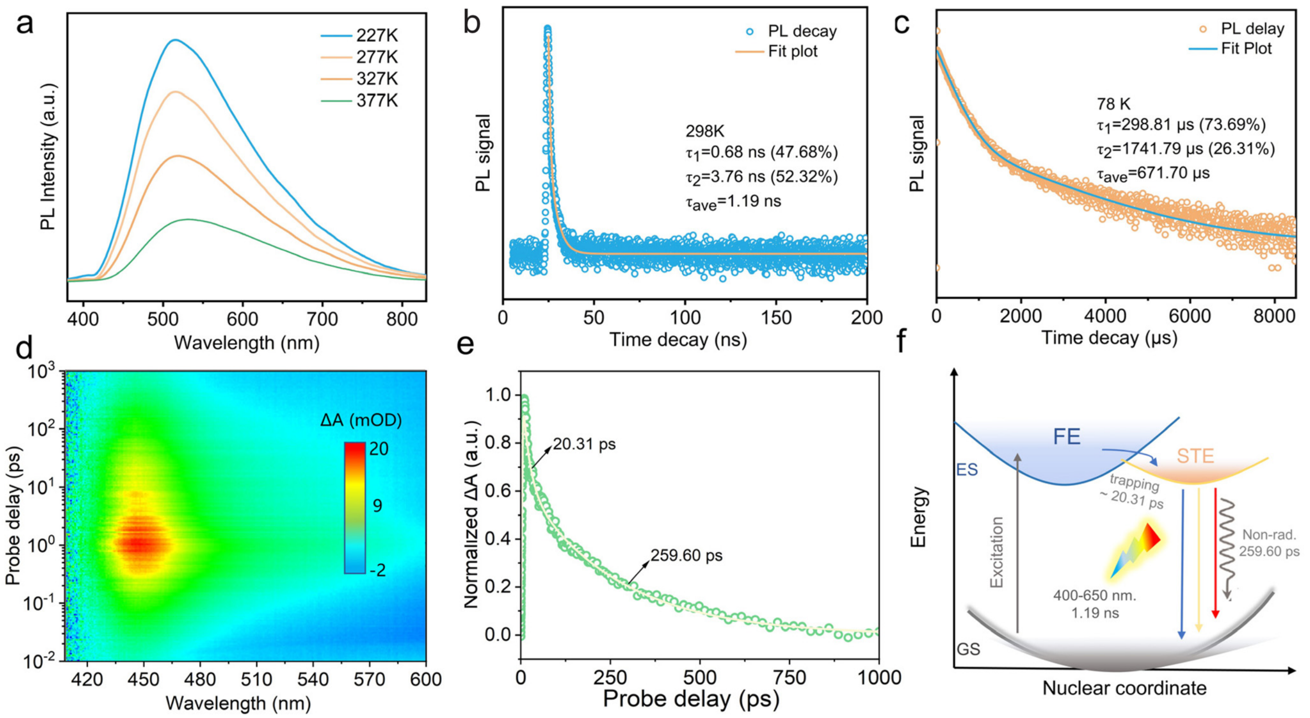

**Fig. 4** (a) Temperature-dependent emission spectra of TJU-19 from 227 to 377 K. (b and c) The photoluminescence decay curve and the fitting plot of TJU-19 at 298 K (b) and 78 K (c). (d) The two-dimensional pseudo-color TA plot of TJU-19. (e) TA kinetics of TJU-19 at 450 nm. (f) Schematic illustration of photoexcited exciton dynamics in TJU-19. ES: excited state; FE: free exciton; GS: ground state.

STEs is present at room temperature.[43] Ultrafast transient absorption (TA) spectroscopy (the pump laser is set as 337 nm, above the band gap, and the range of the probe wavelength is 400–700 nm) was employed to provide deep insight into the photophysical carrier dynamics of TJU-19. The pseudo-color TA spectra of TJU-19 showed broad positive photoinduced absorption ranging from 420 to 600 nm, providing direct evidence for STE formation (Fig. 4d).[2,44] Since the registered TA kinetic profiles show no essential variation at different probe wavelengths within 420–600 nm (Fig. S14†), the TA dynamics of TJU-19 at 470 nm is studied and fitted by the biexponential function equation. The two time constants are determined to be $\tau_1$ of 20.31 ps and $\tau_2$ of 259.60 ps, respectively (Fig. 4e). Among them, the time component $\tau_1$ is attributed to the trapping of free excitons, which is consistent with earlier STE studies.[45] Meanwhile, the time component $\tau_2$ agrees with the non-radiative recombination of STEs, based on the short photoluminescence decay of 0.68 ns.[46] The above-mentioned photophysical studies suggest the overall carrier dynamic process of TJU-19, as shown in Fig. 4f.

## Conclusions

In summary, we introduced an ultrastable member of layered organolead chloride with strong layer corrugation, in which the corrugation amplitude reaches 4.94 Å. Moreover, the coordination architecture demonstrates high robustness in a variety of chemical conditions as well as upon continuous UV irradiation, superior to the (110)-oriented layered perovskites. Therefore, our material features long-term stable broadband emission under ambient conditions, which originates from the exciton self-trapping process that is investigated by a variety of photophysical studies. This work reveals the coordination-assembly as a viable synthetic strategy for organolead halides to retain the intriguing structural features but overcome the lability problems. The broadband STE-based emission and excellent stability make this class of metal halide coordination polymers promising candidates for next-generation solid-state luminescence materials.

## Conflicts of interest

There are no conflicts to declare.

## Acknowledgements

This work was supported by grants from the National Natural Science Foundation of China (21971197 and 22171214), the Shanghai Rising-Star Program (20QA1409500), the Natural Science Foundation of Shanghai (22ZR1463200), the Recruitment of Global Youth Experts by China and the Science & Technology Commission of Shanghai Municipality (19DZ2271500).

# References

1 T. Bai, X. Wang, Z. Wang, S. Ji, X. Meng, Q. Wang, R. Zhang, P. Han, K. L. Han, J. Chen, F. Liu and B. Yang, Highly Luminescent One-Dimensional Organic-Inorganic Hybrid Double-Perovskite-Inspired Materials for Single-Component Warm White-Light-Emitting Diodes, *Angew. Chem., Int. Ed.*, 2023, **62**, e202213240.

2 M. D. Smith and H. I. Karunadasa, White-Light Emission from Layered Halide Perovskites, *Acc. Chem. Res.*, 2018, **51**, 619–627.

3 X. Meng, S. J. Ji, Q. J. Wang, X. C. Wang, T. X. Bai, R. L. Zhang, B. Yang, Y. M. Li, Z. P. Shao, J. K. Jiang, K. L. Han and F. Liu, Organic-Inorganic Hybrid Cuprous-Based Metal Halides for Warm White Light-Emitting Diodes, *Adv. Sci.*, 2022, **9**, 2203596.

4 B. B. Su, S. N. Geng, Z. W. Xiao and Z. G. Xia, Highly Distorted Antimony(III) Chloride $[Sb_2Cl_8]^{2-}$ Dimers for Near-Infrared Luminescence up to 1070 nm, *Angew. Chem., Int. Ed.*, 2022, **61**, e202208881.

5 B. B. Su, J. Jin, Y. H. Peng, M. S. Molokeev, X. B. Yang and Z. G. Xia, Zero-Dimensional Organic Copper(I) Iodide Hybrid with High Anti-Water Stability for Blue-Light-Excitable Solid-State Lighting, *Adv. Opt. Mater.*, 2022, **10**, 2102619.

6 R. Wang, T. Y. Huang, J. J. Xue, J. H. Tong, K. Zhu and Y. Yang, Prospects for metal halide perovskite-based tandem solar cells, *Nat. Photonics*, 2021, **15**, 411–425.

7 J. G. Sun, X. L. Zhang, X. F. Ling, Y. G. Yang, Y. Wang, J. J. Guo, S. Z. Liu, J. Y. Yuan and W. L. Ma, A penetrated 2D/3D hybrid heterojunction for high-performance perovskite solar cells, *J. Mater. Chem. A*, 2021, **9**, 23019–23027.

8 W. C. Xiang, S. Z. Liu and W. Tress, A review on the stability of inorganic metal halide perovskites: challenges and opportunities for stable solar cells, *Energy Environ. Sci.*, 2021, **14**, 2090–2113.

9 L. Chu, S. Zhai, W. Ahmad, J. Zhang, Y. Zang, W. Yan and Y. Li, High-performance large-area perovskite photovoltaic modules, *Nano Res. Energy*, 2022, **1**, e9120024.

10 Z. H. Zhang, S. Y. Yang, J. M. Hu, H. Peng, H. L. Li, P. Y. Tang, Y. R. Jiang, L. B. Tang and B. S. Zou, One-pot synthesis of novel ligand-free tin(II)-based hybrid metal halide perovskite quantum dots with high anti-water stability for solution-processed UVC photodetectors, *Nanoscale*, 2022, **14**, 4170–4180.

11 W. Ma, J. Yin, X. Chen, C. Sun, X. Song and H. Fei, Isoreticular Postsynthetic Modification of Robust Organocopper(I) Halide Hybrids for Enhanced Broad-Band Emission and Turn-On $NH_3$ Sensing, *Chem. Mater.*, 2022, **34**, 4403–4413.

12 F. C. Liu, X. Cai, K. Liu, S. Rafique, F. Behrouznejad, K. J. Bu, X. J. Lu, J. Wang, S. Q. Wu, X. D. Wang, Y. Y. Pan, X. G. Li, Y. C. Cai, J. Q. Zhu, Z. J. Qiu, A. R. Yu, H. Shen, J. L. Wang and Y. Q. Zhan, New Lead-free Organic-Inorganic Hybrid Semiconductor Single Crystals for a UV-Vis-NIR Broadband Photodetector, *ACS Appl. Mater. Interfaces*, 2022, **14**, 33850–33860.

13 X. K. Liu, W. D. Xu, S. Bai, Y. Z. Jin, J. P. Wang, R. H. Friend and F. Gao, Metal halide perovskites for light-emitting diodes, *Nat. Mater.*, 2021, **20**, 10–21.

14 M. D. Smith, A. Jaffe, E. R. Dohner, A. M. Lindenberg and H. I. Karunadasa, Structural origins of broadband emission from layered Pb-Br hybrid perovskites, *Chem. Sci.*, 2017, **8**, 4497–4504.

15 L. L. Mao, Y. L. Wu, C. C. Stoumpos, M. R. Wasielewski and M. G. Kanatzidis, White-Light Emission and Structural Distortion in New Corrugated Two-Dimensional Lead Bromide Perovskites, *J. Am. Chem. Soc.*, 2017, **139**, 5210–5215.

16 E. R. Dohner, A. Jaffe, L. R. Bradshaw and H. I. Karunadasa, Intrinsic White-Light Emission from Layered Hybrid Perovskites, *J. Am. Chem. Soc.*, 2014, **136**, 13154–13157.

17 B. A. Connor, L. Leppert, M. D. Smith, J. B. Neaton and H. I. Karunadasa, Layered Halide Double Perovskites: Dimensional Reduction of $Cs_2AgBiBr_6$, *J. Am. Chem. Soc.*, 2018, **140**, 5235–5240.

18 Y. Jiang, J. Yin and H. Fei, Lowering the dimensionality of cationic lead bromide units in robust coordination polymers for enhanced self-trapped broadband emission, *J. Mater. Chem. C*, 2022, **10**, 13254–13261.

19 X. Song, G. Wei, J. Sun, C. Peng, J. Yin, X. Zhang, Y. Jiang and H. Fei, Overall photocatalytic water splitting by an organolead iodide crystalline material, *Nat. Catal.*, 2020, **3**, 1027–1033.

20 J. A. Christians, P. A. M. Herrera and P. V. Kamat, Transformation of the Excited State and Photovoltaic Efficiency of $CH_3NH_3PbI_3$ Perovskite upon Controlled Exposure to Humidified Air, *J. Am. Chem. Soc.*, 2015, **137**, 1530–1538.

21 E. Mosconi, J. M. Azpiroz and F. De Angelis, Ab Initio Molecular Dynamics Simulations of Methylammonium Lead Iodide Perovskite Degradation by Water, *Chem. Mater.*, 2015, **27**, 4885–4892.

22 M. Kulbak, S. Gupta, N. Kedem, I. Levine, T. Bendikov, G. Hodes and D. Cahen, Cesium Enhances Long-Term Stability of Lead Bromide Perovskite-Based Solar Cells, *J. Phys. Chem. Lett.*, 2016, **7**, 167–172.

23 C. Sun, R. Xi and H. Fei, Organolead Halide-Based Coordination Polymers: Intrinsic Stability and Photophysical Applications, *Acc. Chem. Res.*, 2023, **56**, 452–461.

24 J. Yin, H. Yang and H. Fei, Robust, Cationic Lead Halide Layered Materials with Efficient Broadband White-Light Emission, *Chem. Mater.*, 2019, **31**, 3909–3916.

25 Z. Zhuang, C. Peng, G. Zhang, H. Yang, J. Yin and H. Fei, Intrinsic Broadband White-Light Emission from Ultrastable, Cationic Lead Halide Layered Materials, *Angew. Chem., Int. Ed.*, 2017, **56**, 14411–14416.

26 H. M. Yang, J. L. Yin, X. X. Xu and H. H. Fei, Enhanced intrinsic white-light emission upon near-UV excitation by

crystal engineering of cationic lead bromide layered materials, *J. Mater. Chem. C*, 2019, **7**, 7090–7095.

27 J. Yin, Y. Yu, X. Song, Y. Jiang and H. Fei, Highly Efficient Self-Trapped Bluish White-Light Emission from $[Pb_4Cl_5]^{3+}$ Nodes in a Moisture-Tolerant Metal–Organic Framework, *CCS Chem.*, 2022, **4**, 540–547.

28 C. Peng, X. Song, J. Yin, G. Zhang and H. Fei, Intrinsic White-Light-Emitting Metal-Organic Frameworks with Structurally Deformable Secondary Building Units, *Angew. Chem., Int. Ed.*, 2019, **58**, 7818–7822.

29 B. B. Cui, Y. Han, B. L. Huang, Y. Z. Zhao, X. X. Wu, L. Liu, G. Y. Cao, Q. Du, N. Liu, W. Zou, M. Z. Sun, L. Wang, X. F. Liu, J. P. Wang, H. P. Zhou and Q. Chen, Locally collective hydrogen bonding isolates lead octahedra for white emission improvement, *Nat. Commun.*, 2019, **10**, 5190.

30 Y. Jiang and H. Fei, Efficient and Stable Self–Trapped Blue Emission from a 1D Organolead Chloride Crystalline Material, *Adv. Opt. Mater.*, 2022, **10**, 2102148.

31 Z. Y. Wu, C. M. Ji, Z. H. Sun, S. S. Wang, S. G. Zhao, W. C. Zhang, L. N. Li and J. H. Luo, Broadband white-light emission with a high color rendering index in a two-dimensional organic-inorganic hybrid perovskite, *J. Mater. Chem. C*, 2018, **6**, 1171–1175.

32 G. Kresse, Ab-Initio Molecular-Dynamics for Liquid-Metals, *J. Non-Cryst. Solids*, 1995, **193**, 222–229.

33 G. Kresse and J. Furthmuller, Efficient iterative schemes for ab initio total-energy calculations using a plane-wave basis set, *Phys. Rev. B: Condens. Matter Mater. Phys.*, 1996, **54**, 11169–11186.

34 J. P. Perdew, K. Burke and Y. Wang, Generalized gradient approximation for the exchange-correlation hole of a many-electron system, *Phys. Rev. B: Condens. Matter Mater. Phys.*, 1996, **54**, 16533–16539.

35 G. K. H. Madsen and D. J. Singh, BoltzTraP. A code for calculating band-structure dependent quantities, *Comput. Phys. Commun.*, 2006, **175**, 67–71.

36 H. J. Monkhorst and J. D. Pack, Special Points for Brillouin-Zone Integrations, *Phys. Rev. B: Solid State*, 1976, **13**, 5188–5192.

37 P. A. Barrett, M. A. Camblor, A. Corma, R. H. Jones and L. A. Villaescusa, Synthesis and structure of as-prepared ITQ-4, a large pore pure silica zeolite: The role and location of fluoride anions and organic cations, *J. Phys. Chem. B*, 1998, **102**, 4147–4155.

38 H. Xiao, J. Tahir-Kheli and W. A. Goddard, Accurate Band Gaps for Semiconductors from Density Functional Theory, *J. Phys. Chem. Lett.*, 2011, **2**, 212–217.

39 L. Zhou, J. F. Liao and D. B. Kuang, An Overview for Zero-Dimensional Broadband Emissive Metal-Halide Single Crystals, *Adv. Opt. Mater.*, 2021, **9**, 2100544.

40 E. R. Dohner, A. Jaffe, L. R. Bradshaw and H. I. Karunadasa, Intrinsic White-Light Emission from Layered Hybrid Perovskites, *J. Am. Chem. Soc.*, 2014, **136**, 13154–13157.

41 Z. Y. Wu, C. M. Ji, Z. H. Sun, S. S. Wang, S. G. Zhao, W. C. Zhang, L. N. Li and J. H. Luo, Broadband white-light emission with a high color rendering index in a two-dimensional organic-inorganic hybrid perovskite, *J. Mater. Chem. C*, 2018, **6**, 1171–1175.

42 Y. Y. Ma, H. M. Pan, D. Y. Li, Y. H. Liu, T. Lu, X. W. Lei and Z. H. Jing, Two-dimensional hybrid halide perovskites composed of mixed corner- and edge-shared octahedron as broadband yellow-light emissions, *Inorg. Chem. Commun.*, 2022, **139**, 109411.

43 C. K. Zhou, H. R. Lin, Y. Tian, Z. Yuan, R. Clark, B. H. Chen, L. J. van de Burgt, J. C. Wang, Y. Zhou, K. Hanson, Q. J. Meisner, J. Neu, T. Besara, T. Siegrist, E. Lambers, P. Djurovich and B. W. Ma, Luminescent zero-dimensional organic metal halide hybrids with near-unity quantum efficiency, *Chem. Sci.*, 2018, **9**, 586–593.

44 L. Zhou, J. F. Liao, Z. G. Huang, J. H. Wei, X. D. Wang, H. Y. Chen and D. B. Kuang, Intrinsic Self-Trapped Emission in 0D Lead-Free $(C_4H_{14}N_2)(2)In_2Br_{10}$ Single Crystal, *Angew. Chem., Int. Ed.*, 2019, **58**, 15435–15440.

45 J. Xu, S. Li, C. C. Qin, Z. J. Feng and Y. P. Du, Identification of Singlet Self-Trapped Excitons in a New Family of White-Light-Emitting Zero-Dimensional Compounds, *J. Phys. Chem. C*, 2020, **124**, 11625–11630.

46 Y. Zhang, F. K. Wang, X. Feng, Z. Zhang, K. L. Liu, F. F. Xia, W. X. Liang, X. Z. Hu, Y. Ma, H. Q. Li, G. C. Xing and T. Y. Zhai, Self-Trapped Excitons in 2D $SnP_2S_6$ Crystal with Intrinsic Structural Distortion, *Adv. Funct. Mater.*, 2022, **32**, 2205757.